Light Intensity Distribution in a Photocatalytic Reactor Using Finite Volume

Vishnu K. Pareek
Dept. of Chemical Engineering, Curtin University of Technology, Perth, WA, 6845, Australia

Adesoji A. Adesina
Reactor Engineering and Technology Group, School of Chemical Engineering and Industrial Chemistry, University of New South Wales, NSW, 2052, Australia

DOI 10.1002/aic.10107
Published online in Wiley InterScience (www.interscience.wiley.com).

A conservative variant of discrete ordinate model was used to solve the radiation transport equation. The model prediction was used to assess the effect of wall reflectivity, catalyst loading, and phase function parameter on the light intensity distribution in an annular heterogeneous photocatalytic reactor. For relatively low catalyst loadings, the wall reflectivity strongly influenced the light intensity distribution. However, for an optically thick medium, the wall reflectivity had very little or no effect. The volume-average light intensity distribution decreased rather sharply with the catalyst loading and an opposite trend was obtained for the local volumetric rate of energy absorption (LVREA). However, after the initial sharp increase, the LVREA appeared independent of catalyst loading. For nonreflecting reactor walls, phase function parameter did not show much influence. However, for the specularly reflecting reactor walls and optically thin mediums, a moderate dependency on the phase function parameter was observed.
 AIChE J, 50: 1273–1288, 2004
Keywords: photocatalytic reactor, radiant transport, light intensity distribution, wall reflectivity, light volumetric rate of energy absorption (LVREA)

Introduction

The involvement of radiation is the single most important factor that distinguishes the photochemical/photocatalytic reactor from the conventional thermally activated reactive processes. The rate of initiation (in case of photocatalysis, electron-hole formation) step in photochemical reaction is directly dependent on the light intensity (Cassano et al., 1995). Because the step of electron-hole formation is a fast one (time constant $\approx 10^{15}$ s^{-1}), in a well illuminated reactor, it may be expected that light intensity will not be a rate determining step. However, it is highly difficult to maintain a uniform light intensity within a reactor space and the intensity distribution invariably determines the overall conversion and reactor performance. The radiation transport equation (RTE) that describes the light intensity distribution is an integrodifferential equation, and an exact analytical solution is possible only for highly ideal one-dimensional situations (Carvalho and Farias, 1998). For photocatalytic reactors, however, because of light scattering in the presence of titania particles, it is impossible to find an analytical solution for the RTE. Therefore, to reliably design a photocatalytic reactor, use of new and efficient numerical methods is desired to solve the RTE in the reaction domain of interest. Furthermore, an overall design of the reactor system will require a simultaneous solution of flow equations (e.g., Navier–Stokes equation). It is, therefore, important

Correspondence concerning this article should be addressed to V. K. Pareek at v.pareek@curtin.edu.au.

to investigate the photocatalytic systems using a computational fluid dynamics (CFD) approach so that the effects of flow and radiation attributes can be combined. Most of the current commercial CFD codes use finite-volume scheme to numerically solve the conservation equations. In this study, a finite-volume method—a conservative variant of discrete ordinate model—was used to evaluate the light intensity distribution in an annular photocatalytic reactor.

Carvalho and Farias (1998) presented a state-of-the-art review of various methods developed to numerically solve the RTE. Akehata et al. (1976) were among the first to investigate the light intensity distribution in the heterogeneous reactive systems. They proposed a two-flux method to estimate the light intensity in a bubble-dispersed heterogeneous system. The two-flux method does not use the RTE in an explicit manner but instead the incident radiation is divided into two mutually opposite directions and a radiative energy balance over an infinitesimal slab yields two coupled ordinary differential equations that can be readily solved. The two-flux method is perhaps the simplest approach to investigate the light intensity distribution in the heterogeneous reactive systems. However, the method involves a number of experimentally adjustable parameters, which are difficult to evaluate. Yokota et al. (1977) proposed a stochastic approach to evaluate *local volumetric rate of energy absorption* (LVREA). Spadoni et al. (1978) proposed a Monte Carlo approach to simulate the light scattering in the photocatalytic reactors. They traced the statistically significant light trajectories or bundles emitted from the lamp until the bundles were absorbed or encountered a reactor wall. Yokota and coworkers (1999) extended the Monte Carlo method for the modeling of anisotropic scattering. The "random-walk" model, presented by Yokota et al. (1991), assumed that a scattering light ray could travel along one of the six Cartesian coordinates. Anisotropic scattering was accounted for by assigning a certain probability to one direction and equal probabilities for the other five directions. The model was studied for the analysis of light absorption by a photosynthetic microorganism. The reaction space was divided into a number of finite cubes and the probabilities that light ray would hit a microbe in the cube were analyzed. Pareek et al. (2003a) proposed a similar model by decoupling the effect of in-scattering in the RTE. Recently, a discrete ordinate (DO) model, which has been extensively used for the simulation of radiant energy in furnace design, was proposed for the solution of the radiation transport equation in photocatalytic systems (Romero et al., 1997; Sgalari et al., 1998). In the DO model, the RTE is solved through directional and spatial discretization, giving a set of linear simultaneous equations for the light intensity at various points. The DO model produces relatively accurate results because it does not involve any simplifying assumption other than the discretization of pertinent partial differential equations. However, the DO model does not conserve the radiant energy at the surfaces of complex geometries especially for the anisotropic scattering. Therefore, in most commercial CFD codes, a conservative variant DO model, called the finite-volume (FV) method (Chui and Raithby, 1993), is used, partly because of its ability to exactly conserve the radiative energy and partly because of the fact that most of the commercial CFD softwares are based on the finite-volume scheme.

The light intensity distribution in a photoreactor is determined by a number of factors: (1) the lamp type, (2) the lamp-reactor geometry, (3) the optical properties of medium, and (4) the nature of reactor walls. In this article, we investigate the light intensity distribution in a 14-L pilot scale annular photoreactor, previously described (Pareek et al., 2001), with special emphasis on the effect of reactor wall reflectivity and catalyst loading. In a heterogeneous photocatalytic reactor, the optical properties (such as absorption and scattering coefficients) depend not only on the light wavelength but also on the particle properties. In this study, the effect of these properties was not investigated. However, the proposed model is capable of accounting for the effects of particle properties and light wavelength; this can be achieved by providing more rigorous constitutive relations (as functions of particle properties and light wavelength) for the absorption and scattering coefficients.

Model Development

Radiation transport equation

The formulation of radiation transport equation (RTE) is well established and has been widely used in furnace design application and solar radiation characterization for a fairly long time (Chandrasekhar, 1960). However, application of the RTE to photocatalytic processes is recent (Cassano et al., 1995; Spadoni et al., 1978). After making a radiation balance across a thin slab and substituting appropriate constitutive relations (Cassano et al., 1995; Pareek and Adesina, 2003b), the RTE may be expressed as

$$\frac{dI_\nu(s, \Omega)}{ds} = -\kappa_\nu I_\nu(s, \Omega) - \sigma_\nu I_\nu(s, \Omega) + \frac{1}{4\pi}\sigma_\nu \int_{4\pi} p(\Omega' \rightarrow \Omega) I_\nu(s, \Omega') d\Omega' \quad (1)$$

where the first term on the righthand side represents the loss of photons resulting from absorption, the loss of radiation attributed to out-scattering is accounted for in the second term, and the last term accounts for the gain in the radiation attributed to in-scattering; $p(\Omega' \rightarrow \Omega)$ is the phase function for the in-scattering of photons.

The *incident intensity* at any point from all the directions is given by

$$G_\nu(x, y, z) = \int_{\Omega=0}^{\Omega=4\pi} I_\nu(s, \Omega) d\Omega \quad (2)$$

The local volumetric rate of energy absorption (LVREA) at any point is given by

$$E_{l,\nu}(x, y, z) = \kappa_\nu G_\nu(x, y, z) \quad (3)$$

For photocatalytic applications, only those photons with a wavelength less than or equal to the band gap energy $\lambda_{E_{bg}}$ contribute to the excitation of electrons in the semiconductor particles. A summation may be carried out over this wavelength range to evaluate the total LVREA

$$E_l(x, y, z) = \sum_{\lambda<\lambda_{Eb_g}} E_{l,\nu}(x, y, z) = \sum_{\lambda<\lambda_{Eb_g}} \kappa_\nu G_\nu(x, y, z) \quad (4)$$

Optical properties of reactive medium

Optical properties of the reaction medium play an important role in the overall design of a photoreactor. For example, in homogeneous photochemical reactors, the size of reactor vessel for a given conversion increases exponentially with the optical thickness (defined as $\kappa \times$ distance) (Cassano et al., 1968). In homogeneous systems, only one parameter—the absorption coefficient (κ)—is involved, which may be readily estimated using the Beer–Lambert law. However, for heterogeneous systems, the RTE described in the previous section contains three parameters: the absorption coefficient (κ), the scattering coefficient (σ), and the phase function (p).

Absorption and Scattering Coefficients. Even though theoretical considerations may provide an acceptable expression for the phase function (Siegel and Howell, 1992), because of their coupled nature, determination of κ and σ is not a trivial exercise. The problem is compounded by the integrodifferential nature of the RTE, which prohibits an analytical solution; and a numerical solution demands an a priori estimation of κ and σ. Conventional photometric measurements can, at best, provide a rough estimate of the extinction coefficient ($\beta = \kappa + \sigma$). Most of the approaches suggested in the literature are empirical in nature. For example, Yokota and coworkers (1999) used an iterative (trial-and-error) method to estimate the absorption and scattering coefficients. However, recently, Cabrera et al. (1996) proposed a systematic method to determine the absorption and scattering coefficients of a number of titania photocatalysts. Using a specialized equipment setup, the authors were able to deconvolute scattering and absorption effects from the extinction coefficient. They observed that κ and σ for titania catalyst were strongly influenced by the wavelength of the light. Therefore, the RTE should be solved for the each of the individual wavelength ranges. However, this will make the computations memory-intensive. Consequently, in this study, we have used the wavelength-averaged values of the absorption and scattering coefficients (Romero et al., 1997)

$$\sigma = 3.598 W_{cat} \quad (5)$$

$$\kappa = 0.2758 W_{cat} \quad (6)$$

where σ and κ are the wavelength-averaged scattering and absorption coefficients (m^{-1}) of Aldrich titania particles and W_{cat} is the catalyst loading (g m^{-3}).

Phase Function Parameter. For the isotropic scattering, the phase function parameter (in Eq. 1) has a value of unity. However, for anisotropic scattering, a number of expressions have been reported and each one of them is suitable for specific systems. The widely used phase function is of linear anisotropic form (Fiveland, 1984)

$$p(\theta) = 1 + C \cos(\theta) \quad (7)$$

where p is the scattering phase function to be used in Eq. 1 and $C = 1$, 0, and -1 for forward, isotropic, and backward scattering, respectively. In terms of direction cosines, the phase function may be expressed as

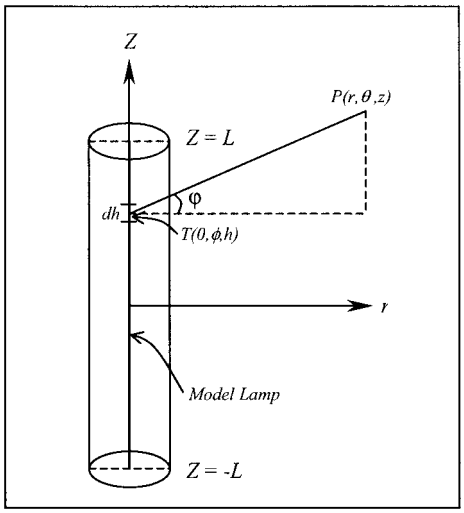

Figure 1. Line source model for lamp emission.

$$p(\Omega^m \rightarrow \Omega^l) = 1 + C(\mu^l\mu^m + \xi^l\xi^m + \eta^l\eta^m) \quad (8)$$

where μ^l, ξ^l, and η^l are the direction cosines of lth direction and μ^m, ξ^m, and η^m are the direction cosines of mth direction.

Radiation source modeling

To solve the RTE for a heterogeneously reactive system, boundary conditions for the light intensity at the light entrance are required. Consequently, an appropriate model for the lamp emission or incidence is needed. Cassano and coworkers (Alfano et al., 1986) reviewed a number of radiation source models proposed by different researchers. The radiation distribution in a given space may be conceptualized in one of two ways. In one approach, termed the *incidence model*, a specific radiant energy distribution (such as an exponential decay) is assumed to exist in the reactor space. In a second class of models referred to as the *emission models*, the rate of photon emission is used to derive an incidence model. All the incidence radiation source models suffer from one common problem: they always need one or more experimentally adjustable parameters. The value of these parameters is dependent on the reactor size and configuration. The radiation source models based on the lamp emission overcome this problem by using the lamp as the focal point of the mathematical description. Broadly speaking, a lamp may be regarded as either an emitting line, a surface, or a volume object. Because of its simplicity, the line source model was used in this study. This model depicts the lamp as a simple emitting line and is schematically illustrated in Figure 1 (Jacob and Dranoff, 1968).

If the number of ν-photons emitted per unit length of the lamp is $K_{\nu 1}$, the number of photons emitted from an element shown in Figure 1 per unit time is

$$dN_\nu = K_\nu dh \quad (9)$$

where $K_{\nu 1} = N_\nu/2L$, N_ν is total number of ν-photons emitted by the lamp, and L is semilength of the lamp.

Table 1. Lamp Parameters

Type	Parameter	Value
Medium-pressure mercury lamp (Primac, AVP06C)	Diameter (D_{lamp})	2.0 cm
	Length (L_{lamp})	15.0 cm
	Average UV production efficiency (between 290 and 400 nm)	22–25%
	Total emission (at 300 W)	10^{-4} einstein s^{-1}

For a specular source, incident light intensity at point P attributed to this element will be obtained by dividing Eq. 9 by the area of the sphere with radius TP ($=\sqrt{r^2 + (z-h)^2}$) (Jacob and Dranoff, 1968)

$$dG_\nu = \frac{K_{\nu l} dh}{4\pi[r^2 + (z-h)^2]} \tag{10}$$

which can be integrated over the entire lamp length and wavelengths to give total incident intensity at point P

$$G = \sum G_\nu = \int_{-L}^{L} \frac{(\sum K_{\nu l})dh}{4\pi[r^2 + (z-h)^2]} = \frac{K_1}{4\pi r}\left[\tan^{-1}\left(\frac{z+L}{r}\right) - \tan^{-1}\left(\frac{z-L}{r}\right)\right] \tag{11}$$

The parameters of the lamp used in this study are reported in Table 1. For this lamp system, the specific emission coefficients ($K_1 = \sum K_{\nu l}$) at 300 W electrical input is calculated to be 6.67×10^{-4} einstein m^{-1} s^{-1}.

Finite-volume method for RTE

Background. In the past, the discrete ordinate (DO) model was a popular choice for solving the RTE (Romero et al., 1997; Sgalari et al., 1998). However, most of the commercial CFD codes use a variation of the DO model, called the finite-volume (FV) model. This revised model automatically allows the conservation of radiant energy, thus overcoming the difficulties encountered in the DO method. In the FV method, the RTE is integrated over both the control angle and the control volume, unlike the DO method, in which the RTE is integrated over the control volume only. In the FV method, apart from the spatial discretization, a relatively new concept of the control angle is involved (Murthy and Mathur, 1998, 2000; Pareek et al., 2003c; Raithby and Chui, 1990). In 2-D, the control angle is simply an angle as shown in Figure 2a and the summation of these angles will be 2π. Figure 2b illustrates a control angle in a 3-D space. For a 3-D control angle

$$\sum_{l=1}^{l=L} \Delta\Omega^l = 4\pi \tag{12}$$

The FV method of solving the RTE can be summarized as follows.

(1) The computational domain is divided into a number of control volumes as in the conventional finite-volume method.

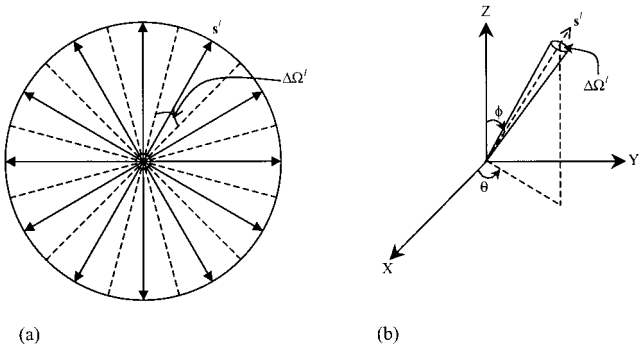

Figure 2. Angular discretization: (a) in 2-D space, (b) in 3-D space.

(2) The solid angle is discretized into a number (L) of finite solid angles or directions.

(3) The RTE is integrated over all control volumes (N) and control angles (L). Applying the boundary conditions gives $N \times L$ linear algebraic equations, which may be solved iteratively. A total of $N \times L$ variables is obtained.

(4) The total incident radiation is calculated at all nodal points (N) by carrying out a vector summation of all directional components.

Mathematical Formulation. Double integration of the RTE in Eq. 1 over an arbitrary control volume (ΔV_P) and a solid angle ($\Delta\Omega^l$) (cf. Figure 3) provides

$$\int_{\Delta\Omega^l}\int_{\Delta V_P} \frac{dI_\nu^l(s,\Omega)}{ds} dV d\Omega = -\int_{\Delta\Omega^l}\int_{\Delta V_P} \beta_\nu I_\nu^l(s,\Omega) dV d\Omega + \int_{\Delta\Omega^l}\int_{\Delta V_P}\left\{\frac{\sigma_\nu}{4\pi}\int_{4\pi} p(\Omega' \rightarrow \Omega) I_\nu(s,\Omega') d\Omega'\right\} dV d\Omega \tag{13}$$

where $\beta_\nu = \kappa_\nu + \sigma_\nu$.

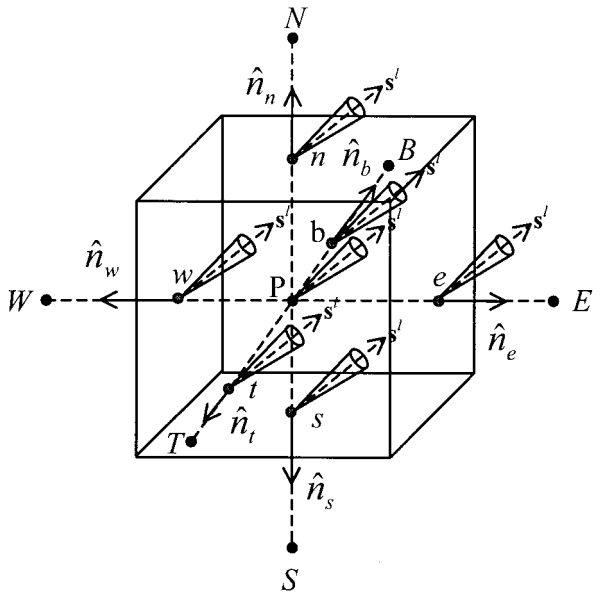

Figure 3. Control volume for the finite-volume (FV) method.

As in the DO method (Romero et al., 1997), if the computational domain is divided into N spatial cells (control volumes or grids) and L solid angles, for each control volume, there are L number of intensities corresponding to L direction vectors. As a result, all the $N \times L$ variables have to be evaluated. The left-hand side (LHS) of Eq. 13 can be rewritten, using the Green theorem, as

$$\text{LHS} = \int_{\Delta\Omega^l}\left\{\int_{\Delta V_P}\frac{dI_\nu^l}{ds}\,dV\right\}d\Omega = \int_{\Delta\Omega^l}\left\{\int_{\Delta V_P}\nabla I_\nu^l\cdot\mathbf{s}^l dV\right\}d\Omega$$
$$= \int_{\Delta\Omega^l}\left\{\int_{\Delta V_P}\nabla\cdot(\mathbf{s}^l I_\nu^l)dV\right\}d\Omega = \int_{\Delta\Omega^l}\left\{\int_{\Delta S_P}(\mathbf{s}^l I_\nu^1)\cdot\hat{\mathbf{n}}dS\right\}d\Omega$$
$$= \int_{\Delta\Omega^l}\left\{\int_{\Delta S_P}(\mathbf{s}^l\cdot\hat{\mathbf{n}})I_\nu^l dS\right\}d\Omega \quad (14)$$

By substituting Eq. 14 in Eq. 13, one obtains

$$\int_{\Delta\Omega^l}\left\{\int_{\Delta S_P}(\mathbf{s}^l\cdot\hat{\mathbf{n}})I_\nu^l dS\right\}d\Omega = -\int_{\Delta\Omega^l}\int\Delta V_P\,\beta_\nu I_\nu^l dV d\Omega$$
$$+\int_{\Delta\Omega^l}\int_{\Delta V_P}\left\{\frac{\sigma_\nu}{4\pi}\int_{4\pi}p(\Omega'\rightarrow\Omega)I_\nu(s,\Omega')d\Omega'\right\}dV d\Omega \quad (15)$$

where $\mathbf{s}^l$ is unit vector along the direction of control angle (lth control angle) and $\hat{\mathbf{n}}$ is a unit vector normal to a surface of the control volume (see Figure 3).

If the number of faces in control volume P is J_P, an integration of Eq. 15 yields

$$\int_{j=1}^{J_P} I_{\nu,j}^l A_j\left(\int_{\Delta\Omega^l}(\mathbf{s}^l\cdot\hat{\mathbf{n}}_j)d\Omega^l\right) = -\beta_\nu I_{\nu,P}^l\Delta V_P\Delta\Omega^l$$
$$+\sigma_\nu\bar{I}_{\nu,P}^l\Delta V_P\Delta\Omega^l \quad (16)$$

where the summation on the LHS has been carried out over all faces (panels) of the control volume P and

$$\bar{I}_{\nu,P}^l = \frac{1}{4\pi}\int_{m=1}^{L}[I_{\nu,P}^m\bar{p}(\Omega^m\rightarrow\Omega^l)\Delta\Omega^m] \quad (17)$$

with $\bar{p}(\Omega^m\rightarrow\Omega^l)$ being the average scattering phase function from control angle m to control angle l

$$\bar{p}(\Omega^m\rightarrow\Omega^l) = \frac{1}{\Delta\Omega^m\Delta\Omega^l}\int_{\Omega=\Delta\Omega^l}\int_{\Omega'=\Delta\Omega^m}p(\Omega^m\rightarrow\Omega^l)d\Omega' d\Omega \quad (18)$$

By applying Eq. 16 to a hexagonal control volume P, shown in Figure 3, one obtains

$$A_e N_e^l I_{\nu,e}^l + A_w N_w^l I_{\nu,w}^l + A_n N_n^l I_{\nu,n}^l + A_s N_s^l I_{\nu,s}^l + A_b N_b^l I_{\nu,b}^l + A_t N_t^l I_{\nu,t}^l$$
$$= -\beta_\nu I_{\nu,P}^l\Delta V_P\Delta\Omega^l + \sigma_\nu\bar{I}_{\nu,P}^l\Delta V_P\Delta\Omega^l \quad (19)$$

where $N_j^l = \int_{\Delta\Omega^l} s^l\cdot\hat{n}_j d\Omega$, $I_{\nu,j}^l$ is intensity at jth face of the control volume, and $\hat{\mathbf{n}}_\mathbf{j}$ is a unit vector normal to jth face of the control volume, with $j = e, w, n, s, b, t$. Also, in this case, $A_e = A_w = \Delta y_p\Delta z_p$, $A_n = A_s = \Delta x_p\Delta z_p$, and $A_t = A_b = \Delta y_p\Delta x_p$.

To permit the evaluation of the incident intensity within the control volume P, the face intensities in Eq. 19 should be related to the node intensities. In most cases the face intensities are treated using an upwind scheme. In this scheme, the face intensities are set to the corresponding upstream nodal values (Chai et al., 1995); the final discretized equations are given by

$$a_P^l I_{\nu,P}^l = a_W^l I_{\nu,W}l + a_E^l I_{\nu,E}^l + a_S^l I_{\nu,S}^l + a_N^l I_{\nu,N}^l$$
$$+ a_T^l I_{\nu,T}^l + a_B^l I_{\nu,B}^l + (\bar{I}_P^l\Delta V_P\Delta\Omega^l) \quad (20)$$

where

$$a_i^l = \max(-A_i N_i^l, 0) \quad \text{with } i = W, E, S, N, T, \text{ and } B \quad (21a)$$

$$a_P^l = \max(A_e N_e^l, 0) + \max(A_w N_w^l, 0) + \max(A_n N_n^l, 0)$$
$$+ \max(A_s N_s^l, 0) + \max(A_t N_t^l, 0) + \max(A_b N_b^l, 0)$$
$$+ \beta_\nu\Delta V_P\Delta\Omega^l \quad (21b)$$

$$N_i^l = \int_{\Delta\Omega^l}\mathbf{s}^l\cdot\hat{\mathbf{n}}_i d\Omega \quad \text{with } i = w, e, s, n, t, \text{ and } b \quad (21c)$$

Equation 20 can be solved iteratively to evaluate $I_{\nu,P}^l$ for all control volumes and control angles. In many cases, an estimate of the wavelength-averaged intensity is sufficient and hence the subscript "ν" may be dropped from I. However, if the spectral distribution of the light intensity is needed, Eq. 20 may be solved separately for all of the wavelength ranges. For photocatalytic processes, the scattering coefficient (σ_ν) and the absorption coefficient (κ_ν) are functions of the wavelength of light (Cabrera et al., 1996), and thus the RTE should be solved for the each wavelength. The total incident intensity may then be obtained from an integration (summation) over the range of applicable wavelengths. However, Romero et al. (1997) have found that only minimal error is introduced by using the computationally less intense wavelength-averaged values of σ_ν and κ_ν to evaluate the overall incident intensity.

Control Angle Overhang. Because control angles ($\Delta\Omega^l$) are defined with respect to global coordinates, the boundaries of a control angle may not align with an arbitrary face of a control volume. This situation is referred as control angle overhang. The control angle overhang is undesired because it creates doubt with respect to the direction of the control angle, whether it is an incoming or outgoing direction. Figure 4a schematically shows a situation in 2-D where all the control

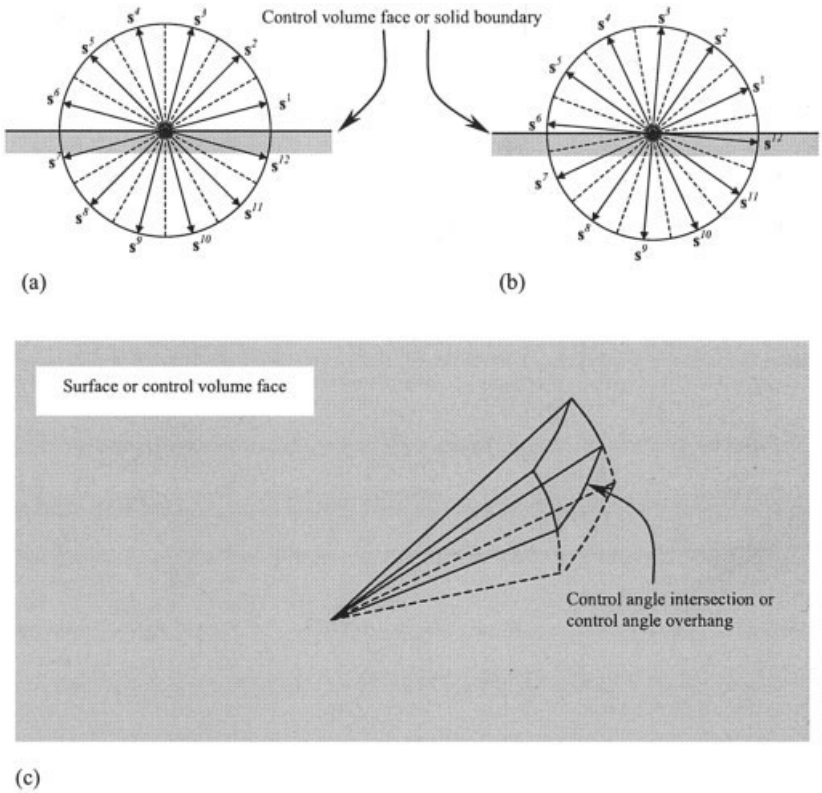

Figure 4. Control volume overhang.

(a) control angles aligned control volume face; thus, no control angle overhang; (b) control angles s^6 and s^{12} intersect the control volume face, resulting into a control angle overhang; (c) control angle overhang in 3-D space.

angles are aligned with a control volume face. Clearly, the solid angles s^1–s^6 correspond to outgoing directions, and incoming directions are represented by the solid angles s^7–s^{12}. In contrast, in Figure 4b, the control volume face is intersected by two of the solid angles, that is, s^6 and s^{12}, and it is not certain whether they represent the incoming or outgoing directions. To overcome the problem of control angle overhang, a number of algorithms have been proposed (Murthy and Mathur, 2000; Raithby, 1999). In general, they involve a further subdivision of those control angles having overhang. The process of the subdivision of control angles into finer control angles is referred to as *pixelation* (Murthy and Mathur, 2000). However, the simplest approach is to do nothing, given that the quantity N_j^l defined in Eq. 21c may automatically assign a direction to overhung control angle and an averaging of all such operations will smooth any inaccuracy that might creep in as a result of that. Chai et al. (1995) obtained good results using the "do-nothing" approach.

Ray Effect. In both FV and DO methods, the calculated radiation intensities tend to concentrate in the discrete direction and starlike contours, centered at the radiation source, are obtained for the light intensity. Figure 5a shows contours of radiation around a 1.0-cm (diameter) lamp in an annular reactor having 10.0-cm outer diameter. In this case, each of the quadrants was divided into two control angles (total of eight directions in the plane). It may be easily noticed that the radiation is very much concentrated in the discrete directions. However, when the quadrants were divided into eight control angles (a total of 32 directions), the ray effect is virtually eliminated, as shown in Figure 5b.

Results and Discussion

To illustrate use of the FV method for estimating the light intensity in a photoreactor, FLUENT 6.0 solver was used to numerically solve the RTE in a pilot-scale photoreactor (Pareek et al., 2001). The characteristics of the lamp used in this study

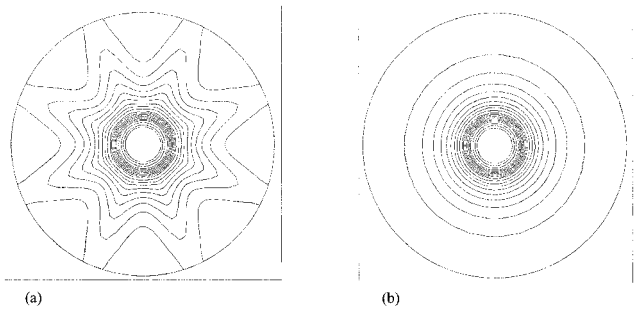

Figure 5. Ray effect in an annular photoreactor (lamp radius = 1.0 cm, reactor radius = 10.0 cm) using the FV method.

(a) Starlike contours were obtained when the direction space was discretized into eight control angles; (b) the ray effect virtually vanished when directional discretization was increased to 32 control angles.

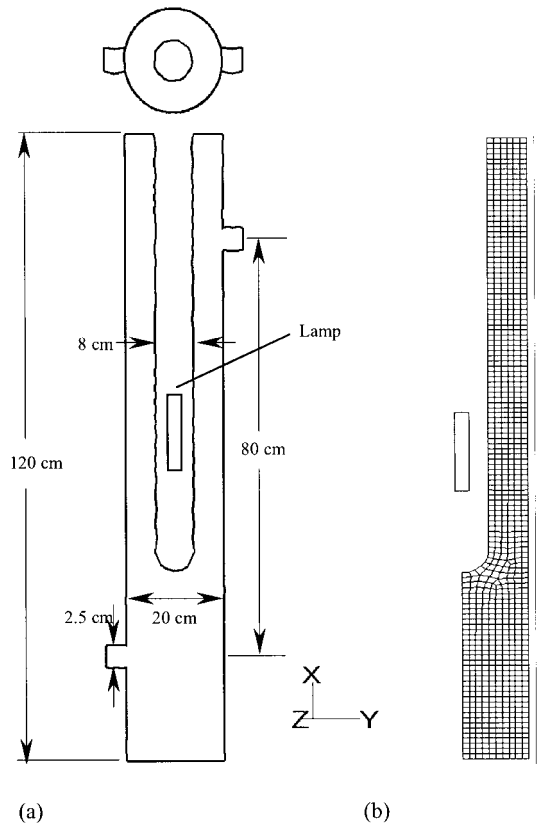

Figure 6. (a) Numerical parameters of the pilot-scale reactor; (b) 2-D grids used in finite-volume radiation calculations.

are listed in Table 1. The simulations were performed for different catalyst loadings and reactor wall reflectivities. The volume-averaged values of scattering and absorption coefficients for titania particles were obtained using Eqs. 5 and 6 (Romero et al., 1997).

Physical picture and solution domain

The computational domain of the annular pilot-scale photoreactor (OD = 20 cm, ID = 8 cm, length = 120 cm, lamp length = 15 cm, lamp OD = 2 cm) used in this study is shown in Figure 6a. The reaction mixture flows in the annular space. The centrally placed UV lamp is cooled by the running water to maintain a uniform reaction temperature as well as to remove the IR fraction of the UV lamp. The UV absorption takes place mainly in the annular reaction space and the absorption within the cooling section is negligible. Therefore, in this analysis, we have discarded the central lamp assembly from a mathematical consideration; instead the light intensity (or incident radiation) at the inner wall was determined using a line source model (Eq. 11).

The axisymmetric nature of the present reactor geometry with respect to radiation distribution allowed a 2-D computational geometry. Furthermore, the mirror symmetry permitted the calculations only in the one half, and the other half could be taken as resolved. Figure 6b shows the final geometry meshed with 861 quadrangle grids. The water inlet and outlet made no contribution in the light intensity and were thus discarded to improve the computational efficiencies.

Boundary conditions

When a certain amount of radiation is incident on a wall, a part of it may be absorbed; a part of it may be transmitted; and the remaining portion may be reflected. Therefore, the following relation holds for a wall

$$a + t + r_{ref} = 1 \tag{22}$$

where a is the absorptivity of the wall, t is its transmittivity, and r_{ref} is the reflectivity. For a blackbody wall, Kirchoff's principle is applicable

$$a = e \tag{23}$$

where e is the emissivity of the walls. By using Eq. 23 in Eq. 22, we have

$$e + t + r_{ref} = 1 \tag{24}$$

Because, in the current reactor configuration, the reactor walls were nontransparent, $t = 0$, Eq. 24 reduces to

$$e + r_{ref} = 1 \tag{25}$$

Given that FLUENT solver accepts values only for the emissivity, for a desired reflectivity r_{ref}, e values should be calculated using Eq. 25.

For setting up the boundary conditions, the following assumptions were made:

(1) The rate of emission of radiation per unit area from the lamp surface is constant.

(2) The reactor surfaces are nonemitting but may be reflecting diffusely or specularly.

Consequently, the boundary conditions may be summarized as follows.

Inner Surface. The incident radiation heat flux is given by

$$G_{in}^{inner} = \int_{\mathbf{sn}>1,inner\_surface} I_{in}\mathbf{s}\cdot\hat{\mathbf{n}}d\Omega \tag{26}$$

where $\mathbf{s}$ is the direction of the incident radiation, $\hat{\mathbf{n}}$ is a unit vector normal to plane of incidence, and Ω is the solid angle.

The net radiative flux leaving the surface is given by

$$G_{out}^{inner} = r_{ref}^{inner}G_{in}^{inner} + \frac{K_1}{4\pi R}\left[\tan^{-1}\left(\frac{x+L}{R}\right) - \tan^{-1}\left(\frac{x-L}{R}\right)\right] \tag{27}$$

where r_{ref}^{inner} is the reflectivity of the inner surface, K_1 is radiant power per unit length of the lamp (einstein m^{-1} s^{-1}), x denotes axial coordinate, R is the radius of the cooling assembly [4 cm in Figure 6(a)], and L is the semilength of the lamp. A *user-*

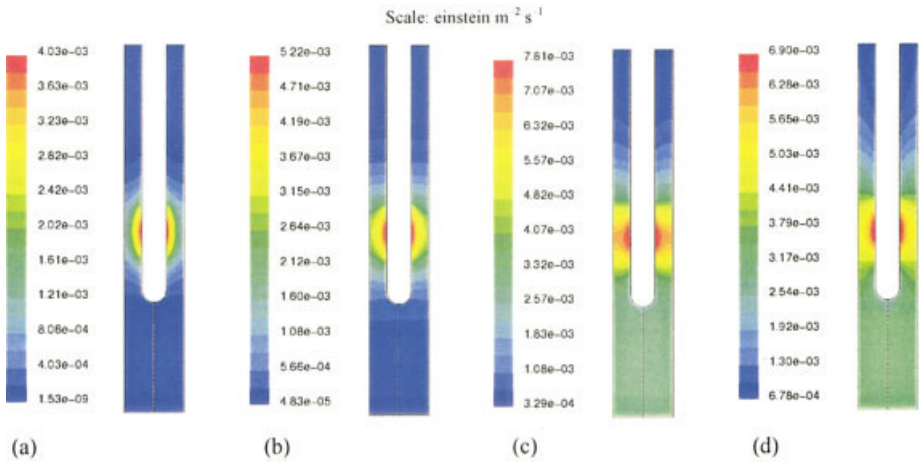

Figure 7. Contours of incident intensity in diactinic medium ($\kappa = \sigma = 0$).

(a) Nonreflecting reactor walls; (b) partially diffusely reflecting reactor walls ($r = 0.5$); (c) diffusely reflecting reactor walls ($r = 1.0$); (d) specularly reflecting reactor walls.

defined function was used to accommodate Eq. 27 in the FLUENT solver.

In a 2-D space, the out-going intensity in all the directions at the lamp surface is calculated by dividing the incident radiation with π (the total of all outgoing directions)

$$I_{out}^{inner} = \frac{G_{out}^{inner}}{\pi} \tag{28}$$

Outer Reactor Walls. The incident intensity at the outer wall is calculated as in Eq. 26

$$G_{in}^{reactor} = \int_{\mathbf{sn}>1, reactor\_surface} I_{in}\mathbf{s}\cdot\mathbf{n}d\Omega \tag{29}$$

The out-going intensity will depend on the reflective properties of the reactor walls. For *diffusely reflecting reactor walls*

$$G_{out}^{reactor} = r_{ref}^{reactor} G_{in}^{reactor} \tag{30}$$

and

$$I_{out}^{reactor} = \frac{G_{out}^{reactor}}{\pi} \tag{31}$$

For *specularly reflecting reactor walls*, the intensity incident from a direction $\mathbf{s}$ is reflected in a direction $\mathbf{s_r}$, expressed as

$$I_{out}^{reactor}(s_r) = I_{in}^{reactor}(s) \tag{32}$$

where the directions $\mathbf{s}$ and $\mathbf{s_r}$ are related to each other according to Snell's law

$$\mathbf{s_r} = \mathbf{s} - 2(\mathbf{s}\cdot\hat{\mathbf{n}})\cdot\hat{\mathbf{n}} \tag{33}$$

Solver parameters

FLUENT's segregated solver was used to perform the numerical experiments. As in other finite-volume calculations, the spatial discretization for the RTE is directly taken from the grid topology. However, the directional discretization for the RTE is supplied to the solver as a user input. In the present study, because of the axisymmetric nature, a relatively smaller directional discretization was used. One quadrant of the grid space in Figure 3 was divided into eight discrete directions (total 32 directions). To avoid control angle overhang, a pixelation of 2×2 was used throughout. A relaxation factor of unity was used to achieve faster convergence. The calculations (iterations) were performed until the intensity residuals were less than or equal to 10^{-6}. A typical convergence history required about 100–200 iterations.

Effect of reactor wall reflectivity

Figure 7 shows the contours of incident intensity in the presence of a diactinic medium ($\kappa = \sigma = 0$) for four different reactor wall types. The calculations were performed only in the right half of the reactor; the other half was mirrored to give a better pictorial representation. With nonreflecting reactor walls in Figure 7a, the intensity, as expected, was mostly concentrated around the lamp area. The incident intensity within the region $|x| \leq 0.10$ m was nearly uniform [coordinate system is dictated in Figure 6b] with intensities in excess of 1×10^{-3} einstein m^{-2} s^{-1}. However, beyond this region, the intensities were less than 2×10^{-9} einstein m^{-2} s^{-1}. This indicates that in the presence of nonreflecting reactor walls, even without any light absorption by the medium, most of the reactor was not illuminated. Therefore, it is recommended to keep the lamp and the reactor length equal if the reflecting walls have to be avoided.

Figure 8 shows the axial and radial profiles of incident intensity corresponding to the contours in Figure 7a. The axial profiles showed a strong symmetry about the line $x = 0$. A slight skewness in the curves toward the left is attributed to the nonalignment of the computational node with $x = 0$ [which

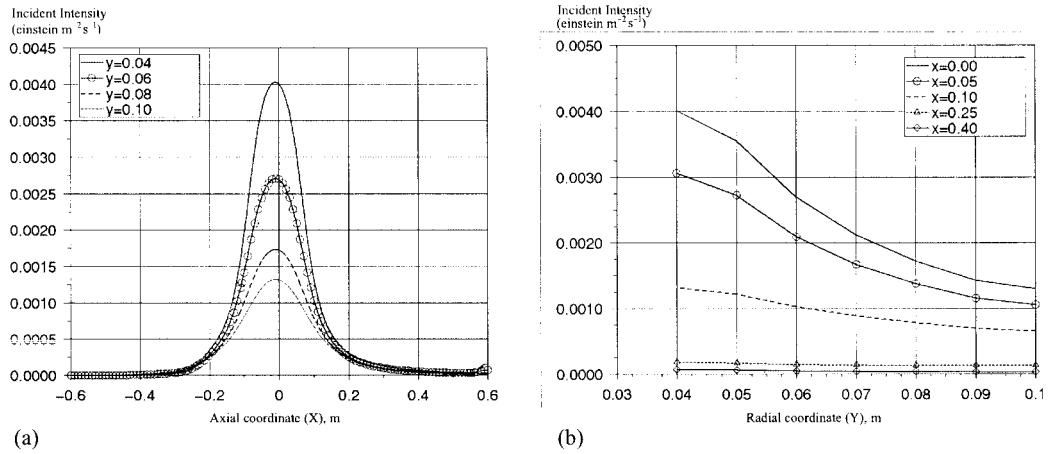

Figure 8. Incident intensity in a diactinic medium ($\kappa = \sigma = 0$) with nonreflecting reactor walls: (a) axial profile; (b) radial profile.

may be ascribed to relatively coarse grids (1×1 cm^2) used in this study]. The maximum intensity was obtained at $x = 0$ and $y = 0.04$ m. It is clear from Figure 8a that incident intensity for a given radial coordinate (y) was nearly uniform in the region of lamp length ($|x| \leq 0.075$). Beyond this region, the intensity dropped rather abruptly, giving nearly a zero value for the points with $|x| \geq 0.25$ m. The radial drop in the intensity in Figure 8b, on the other hand, was more gradual. The gradient of radial intensity decreased with an increase in axial coordinate. For example, the overall gradient in intensity between the inner and outer walls was about 0.04 (einstein m^{-2} s^{-1}) m^{-1} for $x = 0$ and the corresponding value for $x = 0.10$ was only 0.008 (einstein m^{-2} s^{-1}) m^{-1}.

Figure 7b shows the contours of incident intensity for *partially* diffuse reflecting reactor walls ($r_{ref} = 0.5$). The contours were still reasonably symmetrical with respect to the line $x = 0$. The incident intensity, in general, increased at all the points within the reactor. Furthermore, the area of illuminated zone increased slightly. The overall variation (4.8×10^{-5}–5.2×10^{-3} einstein m^{-2} s^{-1}) in incident intensity within the reactor vessel decreased compared with 1.5×10^{-9}–4.0×10^{-3} einstein m^{-2} s^{-1} for the nonreflecting walls. The maximum intensity was still obtained at $x = 0$ and $y = 0.04$ m.

With *completely* diffuse reflecting reactor walls, the area of illumination increased rather drastically. Strong asymmetries appeared in incident intensity contours in Figure 7c. The area $x < 0$ was completely illuminated and the dark zone was confined to a very narrow region $x > 0.40$ m. The maximum intensity near the lamp center showed a slight increase in comparison to that shown with partially reflecting reactor walls [Figure 7b]. However, the minimum intensity showed a significant increase, indicating an increased uniformity in incident intensity distribution.

The uniformity in the radiation distribution was further increased when the reactor walls were made *specularly* reflecting. It is evident from Figure 7d that, in comparison with diffusely reflecting reactor walls, the maximum intensity predictions near the lamp assembly decreased slightly (from 7.8×10^{-3} to 6.9×10^{-3} einstein m^{-2} s^{-1}). However, this decrease was compensated for by an almost 100% increase in the minimum value (from 3.3×10^{-4} to 6.8×10^{-4} einstein m^{-2} s^{-1}).

Figure 9 shows the axial and radial intensity profiles for *specularly* reflecting reactor walls. It is clear from Figure 9a that in the bottom half of the reactor ($x < -0.25$ m), the axial profiles were completely flat. Furthermore, the different profiles merged to give a single line, indicating a completely

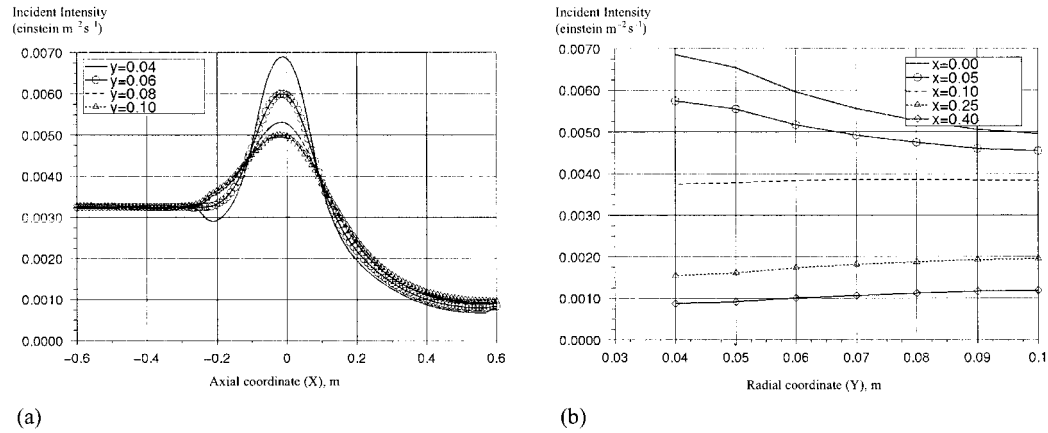

Figure 9. Incident intensity in a diactinic medium ($\kappa = \sigma = 0$) with specularly reflecting reactor walls: (a) axial profile; (b) radial profile.

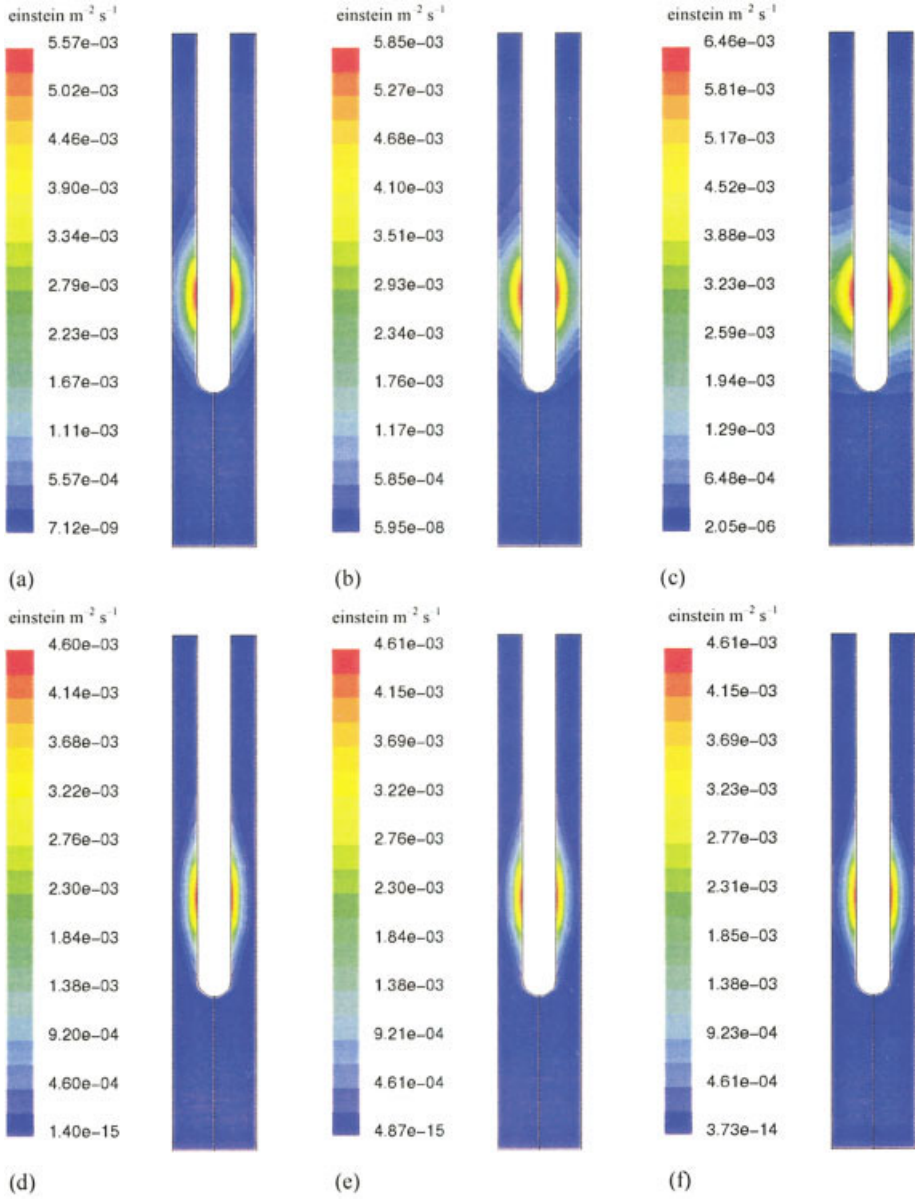

Figure 10. Contours of incident intensity in actinic medium.

(a)–(c): $W_{cat} = 0.01$ g L^{-1} ($\kappa = 2.8$ m^{-1}, $\sigma = 36$ m^{-1}) (a) Nonreflecting reactor walls; (b) partially diffusely reflecting reactor walls ($r = 0.5$); (c) specularly reflecting reactor walls. (d)–(e): $W_{cat} = 0.05$ g L^{-1} ($\kappa = 14$ m^{-1}, $\sigma = 180$ m^{-1}); (d) nonreflecting reactor walls; (e) partially diffusely reflecting reactor walls ($r = 0.5$); (f) specularly reflecting reactor walls.

uniform light intensity distribution in this region. The profile for $y = 0.04$ showed very interesting behavior. In the region $x < -0.25$, this profile was flat and was merged with the other axial profiles but, near the starting of the annular assembly, the profile indicated a slight decrease in the intensity (the minimum was obtained at $x = -0.22$ m) followed by a sharp increase and ultimately a maximum at $x = 0$. Furthermore, in the region $x > 0$, the profile for $y = 0.04$ showed higher intensities than those of other profiles in the region of lamp length ($-0.075 < x < +0.075$). However, beyond the region of lamp length, the incident intensity was significantly diminished relative to that of other profiles. The uniformity in incident intensity below the annular assembly could be attributed to mutually facing specularly reflecting reactor walls. The slight decrease in the incident intensity at the entrance of annular space (for $y = 0.04$ m) was attributed to the shadow of lamp ends, which in this study were assumed to be nonemitting.

Figure 9(b) shows the radial profiles for specularly reflecting reactor walls. Within the lamp length, the incident intensity decreased slightly with radial coordinate, whereas the profile for $x = 0.10$ was nearly flat. Interestingly, the radial profiles for $x > 0.25$ showed a slight increase in incident intensity with radial coordinate. This can be explained from the fact that, in this region, direct irradiation from the lamp was negligible, and most of the illumination in this region was attributed to reflected photons; therefore, a higher incident intensity was expected close to the specularly reflecting reactor walls.

Figure 10 shows contours of incident intensity in an actinic

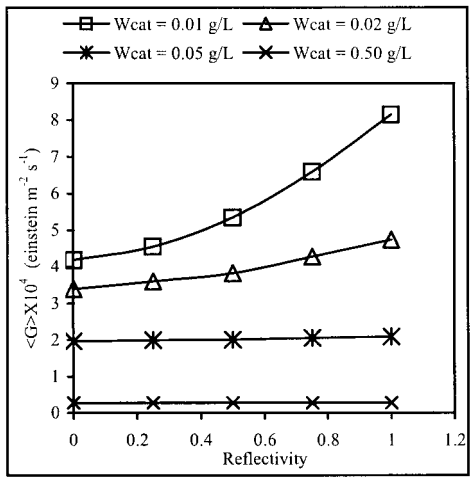

Figure 11. Effect of reactor wall reflectivity on the volume averaged incident radiation (with isotropic phase function).

medium filled with two different titania catalyst loadings, and for three different reactor wall types: nonreflecting, partially reflecting, and specularly reflecting. The completely diffuse reflecting wall gave qualitatively similar results as specularly reflecting walls, therefore, this case was discarded from the discussion. Figure 10a–10c show the contours with a relatively small catalyst loading of 0.01 g L^{-1}. Interestingly, in the cases of nonreflecting and partially reflecting reactor walls [Figure 10a and 10b, respectively], the presence of a small amount of catalyst particles enhanced the overall intensity distribution [compare with Figure 7a and 7b]. The enhancement was more pronounced in the case of nonreflecting walls. The intensity in this case increased by about 40% at the points close to the lamp assembly and nearly 400% at the points far away. However, the increase was not visible for all the points in the reactor space; for the points close to the outer reactor wall, the intensity actually decreased slightly.

Figure 10c shows contours of incident intensity for the same catalyst loading (0.01 g L^{-1}) and with specularly reflecting reactor walls. In comparison with the contours in Figure 7d, the incident intensity decreased at all the points in the reactor vessel. The volume-averaged incident intensity within the reactor was about 5×10^{-4} einstein m^{-2} s^{-1}, which was significantly less than 3×10^{-4} einstein m^{-2} s^{-1} with the diactinic medium. Even with low catalyst loading the uniformly illuminated zone in the bottom of the reactor disappeared. The sharp contrast between the trends in Figures 7d and 10c was because of the increased optical density that decreased the amount of radiation arriving at the reactor walls, and hence decreased the importance of the wall reflectivity.

A further increase in the catalyst loading permitted very little light penetration to the reactor wall. Therefore, the effect of wall reflectivity at catalyst loading 0.05 g L^{-1} diminished significantly and, irrespective of wall reflectivity, contours of essentially the same behavior were obtained in Figure 10d and 10e.

Figure 11 shows volume-averaged incident radiation as a function of the reactor wall reflectivity. The volume averaged incident radiation is defined as

$$\langle G \rangle = \frac{1}{V}\int_0^V G dV = \frac{\sum_{i=1}^{N_c} G_i \Delta V_i}{\sum_{i=1}^{N_c} \Delta V_i} \tag{34}$$

where V is the volume of the reactor, G_i is the incident intensity in the ith control volume (or computational cell), and ΔV_i is the volume of ith control volume. It is clear from the plot (Figure 11) that for $W_{cat} = 0.01$ g L^{-1}, $\langle G \rangle$ was a strong function of the wall reflectivity. However, for $W_{cat} = 0.50$ g L^{-1}, $\langle G \rangle$ was completely independent of the wall reflectivity.

It would therefore seem that wall reflectivity is crucial for a diactinic or an optically thin media. On the other hand, for the optically dense medium, very little light is able to reach the walls, and, consequently, the wall reflectivity is not an important factor. For a photocatalytic reactor, with catalyst loadings in excess of 0.5 g L^{-1}, the effect of reactor wall reflectivity was insignificant; nonetheless, the simulations performed in this study are very useful for low-opacity photochemical reactors (such as photoreactors used for water disinfection), where the effect of wall reflectivity may be quite crucial (Santarelli et al., 1982; Yokota et al., 1983).

Effect of catalyst loading

Because the wall reflectivity was of little importance even at relatively low catalyst loadings (0.05 g L^{-1}), for the higher catalyst loadings, the effect of wall reflectivity was discarded from the numerical considerations. Irrespective of reactor wall reflectivity, Figure 12 shows contours of incident intensity for three different catalyst loadings. It is clear from Figure 12a that for $W_{cat} = 0.1$ g L^{-1}, the illuminated zone was essentially confined to a narrow strip close to the glass assembly and most of the reactor space was rendered as dark. As may be apparent in Figure 12b, when the catalyst loading was increased to 0.5 g L^{-1}, the illuminated strip was narrowed even further, eventually to turn to a thin line in Figure 12c for a catalyst loading of 1.0 g L^{-1}. It is clear from the radiation profiles in Figure 12 that even for the radial points within the lamp zone the radiation intensities were zero just after 2 cm ($y \geq 0.06$ m) from the lamp assembly. Therefore, it may be concluded that for the typical catalyst loadings (1.0–2.0 g L^{-1}) used in the photocatalytic applications, use of annular thickness ($r_o - r_i$) more than about 2 cm may not be useful. Cassano and Alfano (2000) made similar conclusions for a flat-plate photoreactor.

Figure 13a shows the effect of catalyst loading on volume-averaged incident radiation. Clearly, in the absence of photocatalyst, the specular walls gave a very high value of $\langle G \rangle$ ($=3 \times 10^{-3}$ einstein m^{-2} s^{-1}). However, with the introduction of catalyst particles, volume-average intensity dropped rather abruptly. After the catalyst loading of 0.02 g L^{-1}, different curves merged with each other and no meaningful observations could be made for the other two wall reflectivities (nonreflecting and partially reflecting). Therefore, the behaviors shown by these two cases were redrawn in Figure 13b on a more sensitive x–y scale. The volume-averaged intensity for the partially reflecting reactor walls decreased sharply with the catalyst loading. Interestingly, the volume-averaged intensity for the nonreflecting reactor walls showed a minor increase initially and a maximum was obtained at 0.01 g L^{-1}. This initial increase in the incident intensity can be ascribed to in-scattering effects attributed to titania particles. This is consistent with the earlier

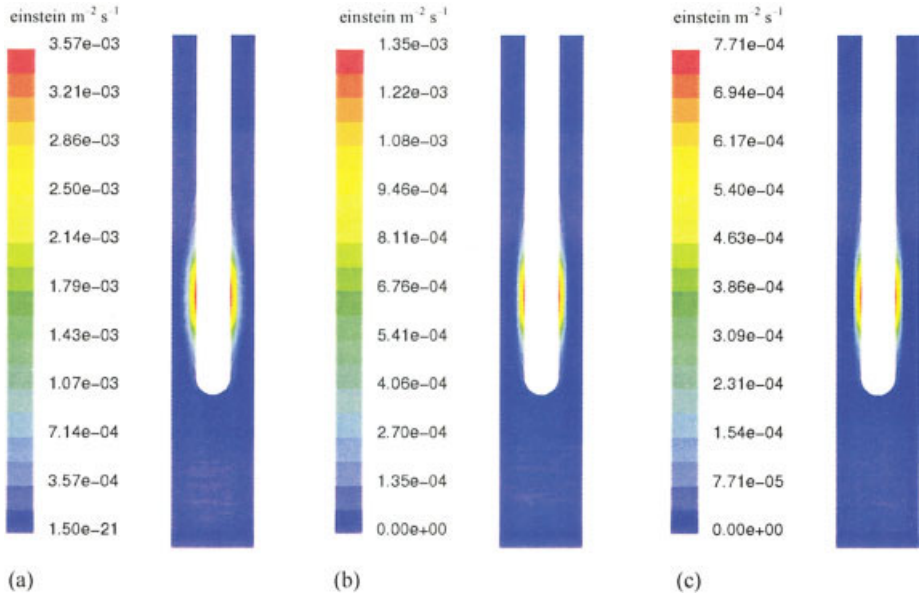

Figure 12. Contours of incident radiation with high optical density: (a) W_{cat} = 0.10 g L^{-1} (κ = 28 m^{-1}, σ = 360 m^{-1}); (b) W_{cat} = 0.50 g L^{-1} (κ = 140 m^{-1}, σ = 1800 m^{-1}); (c) W_{cat} = 1.0 g L^{-1} (κ = 280 m^{-1}, σ = 3600 m^{-1}).

study of Cassano and coworkers (Romero et al., 1997), albeit in an annular photoreactor of different size. However, beyond this point, the intensity decreased quite progressively and eventually for $W_{cat} \geq 0.05$ g L^{-1}, the two curves in Figure 13b merged. Also drawn in Figure 13b are the experimental observations (from Pareek et al., 2003a). Because the walls of the pilot-scale photoreactor were not polished, the variation in incident intensity with catalyst loading could be best approximated by the model predictions using partially reflecting reactor walls ($r_{ref} = 0.5$).

Information on incident intensity distribution was then used to calculate the volume-averaged local volumetric rate of energy absorption (LVREA) using Eqs. 3 and 4. Volume-averaged values of LVREA may then be computed using

$$\langle LVREA \rangle = \frac{\int_{i=1}^{N_c} E_{l,i} \Delta V_i}{\int_{i=1}^{N_c} \Delta V_i} \tag{35}$$

Figure 14a plots the volume averaged LVREA against the catalyst loading for the three different types of reactor walls. Initially, $\langle LVREA \rangle$ increased with the catalyst loading with the specularly reflecting reactor walls giving relatively higher values of $\langle LVREA \rangle$. However, after $W_{cat} = 0.50$ g L^{-1} the three curves in Figure 14(a) merged with each other and $\langle LVREA \rangle$ became constant, irrespective of catalyst loadings. Therefore, from the perspective of radiation absorption, the catalyst concentrations higher than this ($W_{cat} = 0.50$ g L^{-1}) should not be important. In reality, however, the catalyst loadings greater

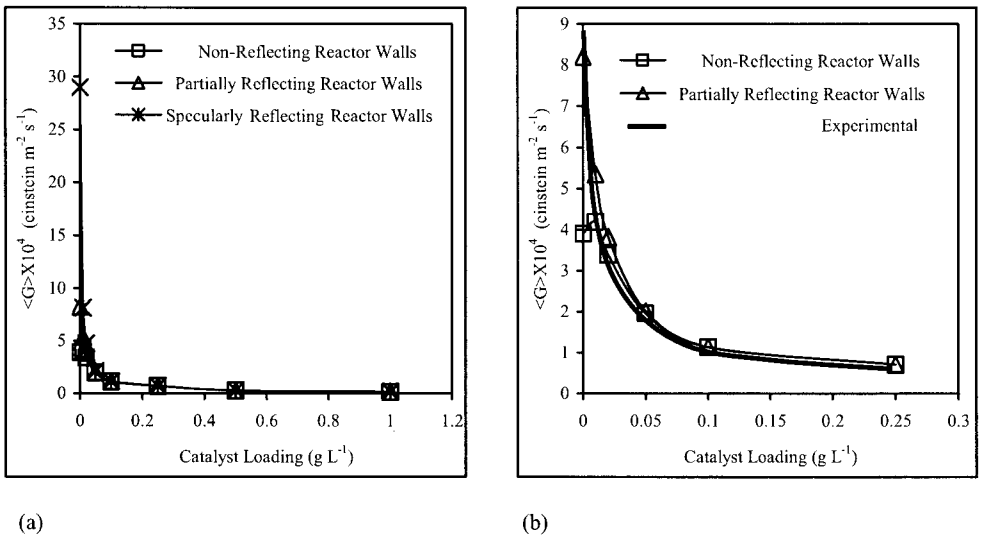

Figure 13. Effect of catalyst loading on the volume-averaged incident radiation (with isotropic phase function): (a) complete range; (b) on a more sensitive scale.

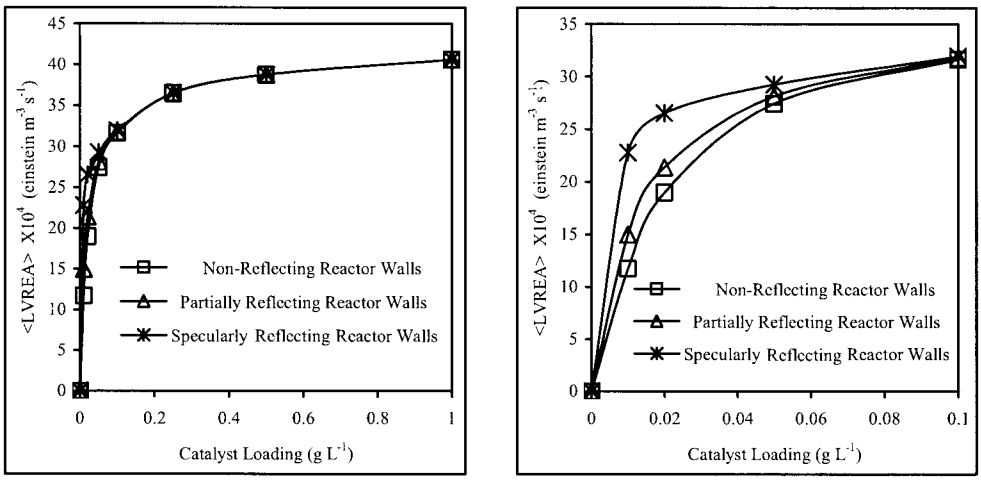

Figure 14. Effect of catalyst loading on the volume-averaged LVREA (using isotropic phase function): (a) with complete range; (b) on a more sensitive scale.

than 2 g L^{-1} have been found to yield optimum results (Cassano and Alfano, 2000). This is because the optimum catalyst loading is not determined solely by the optical properties of the reacting medium. Electrochemical factors, such as pH and ionic strength, may cause agglomeration and possibly change the optical characteristics of the medium itself. Furthermore, properties inherent to catalytic activity other than the photoabsorption rates have strong influence on the reaction rates (Cassano and Alfano, 2000). Therefore, it is not possible to predict an optimum catalyst loading from radiation absorption rate calculations alone. Nonetheless, the CFD approach to modeling of incident intensity distribution is useful in parametric investigation for the specific photocatalytic processes.

To investigate the effect of wall reflectivity more clearly, the data in Figure 14a were plotted on a more sensitive scale in Figure 14b. Clearly, for low catalyst loadings, the specularly reflecting reactor walls gave superior results. However, for higher catalyst loading (or more realistic values used in photocatalysis) the three walls gave essentially the same $\langle LVREA \rangle$. Therefore, it may be concluded that in an annular photoreactor with highly absorbing and scattering photocatalyst, the effect of reactor walls may be discarded from the reactor design and analysis. However, for optically thin mediums, the effect of wall reflectivity cannot be neglected.

Effect of phase function parameter

The in-scattering term in radiation transport equation (RTE) (Eq. 1) requires a phase function parameter. There are three different scattering situations: (1) isotropic scattering, (2) anisotropic forward scattering, and (3) anisotropic backward scattering. Experimental measurement of the phase function is very difficult because of geometrical dependency of in-scattering. However, some mathematical considerations may reduce this difficulty (Siegel and Howell, 1992). For isotropic scattering, phase function parameter is simply unity

$$p(\Omega' \rightarrow \Omega) = 1 \tag{36}$$

Cassano and Alfano (2000) investigated the dependency of light intensity distribution on the phase-function parameter and reported that the specular reflection model (Siegel and Howell, 1992) (which is a highly anisotropic phase function with a very acute peak in the forward direction) may hardly be considered a good approximation for the titania particles (Cassano and Alfano, 2000). The diffuse reflectance model (which has a smooth anisotropy and significant backscattering as the prevailing direction) appeared to be more applicable to titania particles. From their calculations in a flat-plate photocatalytic reactor, the authors concluded that the isotropic scattering gave better comparison with the experimental observations.

Because of the mathematical simplicity and ability to model both forward and backward scattering in the present study, a linear anisotropic phase function was used (FLUENT 2001)

$$p(\Omega' \rightarrow \Omega) = 1 + C(\mathbf{s}' \cdot \mathbf{s}) \tag{37}$$

where C is a constant; $C = +1$ for forward scattering, $C = 0$ for isotropic scattering, and $C = -1$ for backward scattering.

Figure 15 shows plots of volume-averaged incident radiation as a function of C in the presence of nonreflecting reactor walls for four different catalyst loadings. The maximum difference in the intensity between any of two extremes of scattering ($C = -1$ and $+1$)

$$\delta G = \frac{|\langle G \rangle_{C=+1} - \langle G \rangle_{C=-1}|}{\langle G \rangle_{C=-1}} \times 100 \tag{38}$$

was less than 2.5%, indicating the relatively low sensitivity of the scattering phase function toward the light intensity distribution. Pasquali et al. (1996) made similar observations using a Monte Carlo simulation approach. However, this is not a general conclusion for all the scattering phase functions. For example, Romero et al. (1997) investigated different phase functions and observed that the difference between the predic-

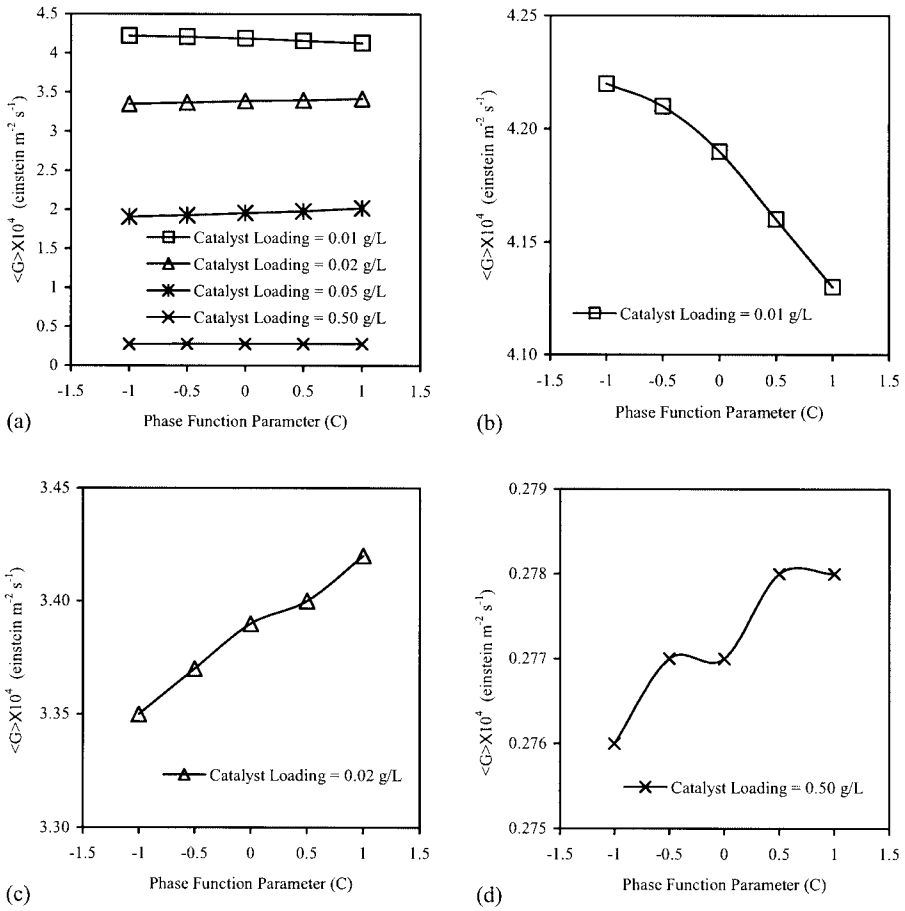

Figure 15. Effect of linear phase function parameter (with nonreflecting reactor walls): (a) for four different catalyst loadings; (b) for W_{cat} = 0.01 g L^{-1}; (c) for W_{cat} = 0.02 g L^{-1}; (d) for W_{cat} = 0.50 g L^{-1}.

tions using diffuse reflectance and specular reflectance models may be as high as 70%. However, the authors found very little disagreement between the values calculated using the diffuse reflectance and isotropic models.

For the data shown in Figure 15b, δG was a negligible 2.1%. The phase function parameter showed an even smaller dependency at higher catalyst loadings in Figure 15d with a δG value of 1.0%. For $W_{cat} = 0.01$ g L^{-1}, $\langle G \rangle$ decreased with C and for other catalyst loadings an opposite trend was obtained. This behavior can be explained from the fact that C is a direct measure of the scattering direction: an increase in C increases the forward scattering, and a more uniform incident intensity is expected. Furthermore, the effect of C will be more pronounced at higher catalyst loadings (optically thick medium). Therefore, an increase in C, for higher catalyst loadings, enhanced the overall uniformity in radiation, thus increasing the volume averaged intensity $\langle G \rangle$. However, for low catalyst loading, an increase in C allowed a portion of the incident photons to arrive at nonreflecting reactor walls, resulting in loss of active photons; therefore, a slight decrease in $\langle G \rangle$ was predicted.

To see the effect of wall reflectivity on the choice of phase function parameter, the calculations of Figure 15 were repeated with specularly reflecting reactor walls and the results are shown in Figure 16. Interestingly, in this case, $\langle G \rangle$ showed a stronger sensitivity toward the phase-function parameter with the difference δG being as high as 10.1% [for the data in Figure 16c]. Unlike the case with nonreflecting reactor walls, an increase in C, with specularly reflecting reactor walls, always resulted in an increase in $\langle G \rangle$. The increase in $\langle G \rangle$ for higher catalyst loading can be explained in a similar manner as with nonreflecting reactor walls. As with nonreflecting reactor walls, low catalyst loadings permitted some photons to arrive at reactor walls, but no loss of photons occurred; therefore, in this case, the incident intensity increased with C, even for low catalyst loadings.

Conclusions

A conservative variant of discrete ordinate model available in FLUENT was used to assess the effect of wall reflectivity, catalyst loading, and phase function parameter on the light intensity distribution. For relatively low catalyst loadings, the wall reflectivity strongly influenced the light intensity distribution. However, for an optically thick medium, the wall reflectivity had very little or no effect. The volume-average light intensity distribution decreased rather sharply with the catalyst loading and an opposite trend was obtained for LVREA. However, after the initial sharp increase, the LVREA remained invariant of catalyst loading. For nonreflecting reactor walls, phase function parameter did not show much influence. However, for the specularly reflecting reactor walls and optically

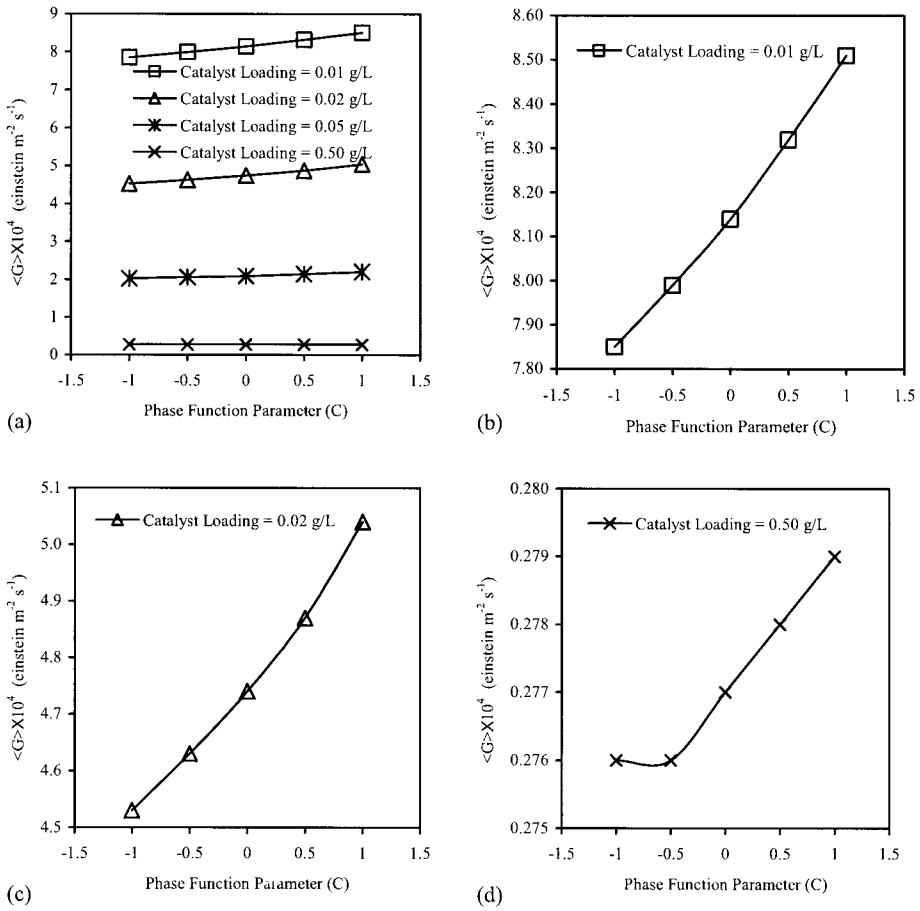

Figure 16. Effect of linear phase function parameter (with specularly reflecting reactor walls): (a) for four different catalyst loadings; (b) for W_{cat} = 0.01 g L^{-1}; (c) for W_{cat} = 0.02 g L^{-1}; (d) for W_{cat} = 0.50 g L^{-1}.

thin mediums, a moderate dependency on the phase function parameter was obtained.

The advantage of the proposed approach is that it can easily be extended to predict light intensity in more complex reactor geometries such as parabolic, elliptical, and multiple lamp photoreactors. Because this approach is based on general computational fluid dynamics, the hydrodynamic and radiation transport equations can be solved concurrently to allow more accurate photoreactor designs. The predicted LVREA data can be used to calculate the reaction rates at various reactor points and can be used in the continuity equation to predict the overall conversion (Pareek et al., 2003c).

Notation

A_j = area of jth face of control volume, m^2
a_J^l = parameters defined in Eq. 21, with $J = E, W, N, S, T, B$, and P
e = emissivity
C = phase function parameter
E_{bg} = band gap energy, J
E_l = local volumetric rate of energy absorption, einstein m^{-3} s^{-1}
G = total incident radiation, einstein m^{-2} s^{-1}
h = axial coordinate of an element on lamp, m
I = radiation intensity, einstein m^{-2} s^{-1} sr^{-1}
K_l = total lamp specific emission parameter, einstein m^{-1} s^{-1}
$K_{\nu l}$ = rate of photons emitted per unit length of lamp, einstein m^{-1} s^{-1}
L = semilength of lamp, m; also total number of control angles, dimensionless
N = total number of control volumes
N_ν = number of ν-photons emitted from lamp per unit time, einstein s^{-1}
$N_j^l = \int_{\Delta\Omega^l} \mathbf{s^l} \cdot \hat{\mathbf{n}}_j d\Omega$
$\hat{\mathbf{n}}_j$ = unit vector normal to jth control volume surface
$p(\Omega \rightarrow \Omega')$ = phase function for scattering in RTE, dimensionless
r = radial coordinate, m
r_{ref} = reflectivity
R = radius of lamp-cooling assembly, m
R_l = outer radius of reactor, m
$\mathbf{s}^l$ = unit vector in the lth direction, m
t = transmittivity
W_{cat} = catalyst loading, g m^{-3}
x, y, z = Cartesian coordinate, m

Greek letters

ΔV_p = volume of pth control-volume, m^3
$\Delta\Omega^l$ = solid angle corresponding to lth control angle, steradian (sr)
Ω = solid angle, sr
β = $(\kappa + \sigma)$, extinction coefficient, m^{-1}
ϕ = angular coordinate of an element of lamp, also equatorial angle, radian
θ = angular coordinate, radian
σ = scattering coefficient, m^{-1}

κ = absorption coefficient, m^{-1}
λ = wavelength of radiation, m
ν = frequency of radiation, s^{-1}
μ^l, ξ^l, η^l = direction cosines

Subscripts

e, w, s, n, t, b = east, west, south, north, top, and bottom faces of a control volume
E, W, S, N, T, B = east, west, south, north, top, and bottom neighbors of a control volume P
P = a general control volume
ν = frequency of radiation
θ = angular component of a vector

Superscript

l = lth control angle

Acronyms

DO = discrete ordinate
FV = finite volume
LVREA = local volumetric rate of energy absorption, einstein $m^{-3}\ s^{-1}$
RTE = radiation transport equation

Literature Cited

Akehata, T., K. Ito, and A. Inokawa, "Light Intensity Profiles in Bubble-Dispersed Systems. An Approach to Analysis of Heterogenous Photoreactors," *Kagaku Kogaku Ronbunshu*, **2**, 583 (1976).

Alfano, O. M., R. L. Romero, and A. E. Cassano, "Radiation Field Modeling in Photoreactors. I. Homogenous Media," *Chem. Eng. Sci.*, **41**, 421 (1986).

Cabrera, M. I., O. M. Alfano, and A. E. Cassano, "Absorption and Scattering Coefficient of Titanium Dioxide Particulate Suspensions in Water," *J. Phys. Chem.*, **100**, 20043 (1996).

Carvalho, M. G., and T. L. Farias, "Modelling of Heat Transfer in Radiating and Combustion Systems," *Trans IChemE, Part A*, **76**, 175 (1998).

Cassano, A. E., and O. M. Alfano, "Reaction Engineering of Suspended Solid Heterogeneous Photocatalytic Reactors," *Catal. Today*, **58**, 167 (2000).

Cassano, A. E., C. A. Martin, R. J. Brandi, and O. M. Alfano, "Photoreactor Analysis and Design: Fundamentals and Applications," *Ind. Eng. Chem. Res.*, **34**, 2155 (1995).

Cassano, A. E., P. L. Silveston, and J. M. Smith, "Photochemical Reaction Engineering," *Ind. Eng. Chem.*, **59**, 18 (1968).

Chai, J. C., G. Parthasarathy, H. S. Lee, and S. V. Patankar, "Finite Volume Radiative Heat Transfer Procedure for Irregular Geometries," *J. Thermophys. Heat Transfer*, **9**, 410 (1995).

Chandrasekhar, S., *Radiative Transfer*, Dover Publishers, New York (1960).

Chui, E. H., and G. D. Raithby, "Computation of Radiant Heat Transfer on a Non-Orthogonal Mesh Using the Finite-Volume Method," *Numerical Heat Transfer, Part B*, **23**, 269 (1993).

Fiveland, W. A., "Discrete-Ordinates Solutions of the Radiative Transport Equation for Rectangular Enclosures," *J. Heat Transfer*, **106**, 699 (1984).

FLUENT 6.0 Users Guide, Fluent USA, Lebanon, NH (2001).

Jacob, S. M., and J. S. Dranoff, "Design and Analysis of Perfectly Mixed Photochemical Reactors," *Chem. Eng. Prog. Symp. Ser.*, **64**, 54 (1968).

Murthy, J. Y., and S. R. Mathur, "Radiative Heat Transfer in Axisymmetric Geometries Using an Unstructured Finite-Volume Method," *Numerical Heat Transfer, Part B*, **33**, 397 (1998).

Murthy, J. Y., and S. R. Mathur, "A Finite-Volume Scheme for Radiative Heat Transfer in Semitrnsparent Media," *Numerical Heat Transfer, Part B*, **37**, 25 (2000).

Pareek, V. K., M. P. Brungs, and A. A. Adesina, "Continuous Process for Photodegradation of Industrial Bayer Liquor," *Ind. Eng. Chem. Res.*, **40**, 5120 (2001).

Pareek, V. K., and A. A. Adesina, "Analysis of Photocatalytically Reactive Systems: Kinetic Modelling and Reactor Design Via Computational Fluid Dynamics (CFD)," in *Handbook of Photochemistry and Photobiology*, H. S. Nalwa, ed., American Scientific Publishers, Stevenson Ranch, CA (2003b).

Pareek, V. K., M. P. Brungs, and A. A. Adesina, "A New Simplified Model for Light Scattering in Photocatalytic Reactors," *Ind. Eng. Chem. Res.*, **42**, 26 (2003a).

Pareek, V. K., S. J. Cox, M. P. Brungs, B. Young, and A. A. Adesina, "Computational Fluid Dynamic (CFD) Simulation of a Pilot-Scale Annular Bubble Column Photocatalytic Reactor," *Chem. Eng. Sci.*, **58**, 959 (2003c).

Pasquali, M., F. Santarelli, J. F. Porter, and P.-L. Yue, "Radiative Transfer in Photocatalytic Systems," *AIChE J.*, **42**, 532 (1996).

Raithby, G. D., "Evaluation of Discretization Errors in Finite-Volume Radiant Heat Transfer Predictions," *Numerical Heat Transfer, Part B*, **36**, 241 (1999).

Raithby, G. D., and E. H. Chui, "A Finite-Volume Method for Predicting a Radiant Heat Transfer in Enclosures with Participating Media," *J. Heat Transfer*, **112**, 415 (1990).

Romero, R. L., O. M. Alfano, and A. E. Cassano, "Cylindrical Photocatalytic Reactors. Radiation Absorption and Scattering Effects Produced by Suspended Fine Particles in an Annular Space," *Ind. Eng. Chem. Res.*, **36**, 3094 (1997).

Santarelli, F., C. Stramigioli, G. Spiga, and M. N. Özisik, "Effects of Scattering and Reflection of Radiation on Batch Photochemical Reaction in a Slab Geometry," *Int. J. Heat Mass Transfer*, **25**, 57 (1982).

Sgalari, G., G. Camera-Roda, and F. Santarelli, "Discrete Ordinate Method in the Analysis of Radiative Transfer in Photocatalytically Reacting Media," *Int. Commun. Heat Mass Transfer*, **25**, 651 (1998).

Siegel, R., and J. R. Howell, *Thermal Radiation Heat Transfer*, Hemisphere Publishers, Washington, DC (1992).

Spadoni, G., E. Bandini, and F. Santarelli, "Scattering Effects in Photosensitized Reactions," *Chem. Eng. Sci.*, **33**, 517 (1978).

Yokota, T., S. Cesur, H. Suzuki, H. Baba, and Y. Takahata, "Anisotropic Scattering Model for Estimation of Light Absorption Rates in Photoreactor with Heterogeneous Medium," *J. Chem. Eng.*, **32**, 314 (1999).

Yokota, T., T. Iwano, and T. Tadaki, "Light Absorption Rate in a Heterogeneous Photochemical Reactor," *Kagaku Kogaku Ronbunshu*, **3**, 248 (1977).

Yokota, T., H. Sugimori, K. Maita, and T. Tadaki, "Light Absorption Rate in a Photochemical Reactor with Diffuse Reflectors," *Kagaku Kogaku Ronbunshu*, **9**, 339 (1983).

Yokota, T., K. Yashima, T. Takigawa, and K. Takahashi, "A New Random-Walk Model for Assessment of Light Energy Absorption by a Photosynthetic Microorganism," *J. Chem. Eng.*, **24**, 558 (1991).

Manuscript received May 2, 2003, and revision received July 11, 2003.